



Article

High Thermoelectric Performance of a Novel γ -PbSnX₂ (X = S, Se, Te) Monolayer: Predicted Using First Principles

Changhao Ding, Zhifu Duan, Nannan Luo, Jiang Zeng, Wei Ren *, Liming Tang and Keqiu Chen *

Department of Applied Physics, School of Physics and Electronics, Hunan University, Changsha 410082, China; dingchanghao@hnu.edu.cn (C.D.); dzf1197333134@hnu.edu.cn (Z.D.); luonn@hnu.edu.cn (N.L.); jiangzeng@hnu.edu.cn (J.Z.); lmtang@hnu.edu.cn (L.T.)

* Correspondence: weiren@hnu.edu.cn (W.R.); keqiuchen@hnu.edu.cn (K.C.);

Tel.: +86-15124553667 (W.R.); +86-0731-88821829 (K.C.)

Abstract: Two-dimensional (2D) group IV metal chalcogenides are potential candidates for thermoelectric (TE) applications due to their unique structural properties. In this paper, we predicted a 2D monolayer group IV metal chalcogenide semiconductor γ -PbSn₂ (X = S, Se, Te), and first-principles calculations and Boltzmann transport theory were used to study the thermoelectric performance. We found that γ -PbSnX₂ had an ultra-high carrier mobility of up to $4.04 \times 10^3 \text{ cm}^2 \text{ V}^{-1} \text{ s}^{-1}$, which produced metal-like electrical conductivity. Moreover, γ -PbSn₂ not only has a very high Seebeck coefficient, which leads to a high power factor, but also shows an intrinsically low lattice thermal conductivity of 6–8 W/mK at room temperature. The lower lattice thermal conductivity and high power factors resulted in excellent thermoelectric performance. The *ZT* values of γ -PbSnS₂ and γ -PbSnSe₂ were as high as 2.65 and 2.96 at 900 K, respectively. The result suggests that the γ -PbSnX₂ monolayer is a better candidates for excellent thermoelectric performance.

Keywords: thermoelectric properties; first principles; Boltzmann transport equation



Citation: Ding, C.; Duan, Z.; Luo, N.; Zeng, J.; Ren, W.; Tang, L.; Chen, K. High Thermoelectric Performance of a Novel γ -PbSnX₂ (X = S, Se, Te) Monolayer: Predicted Using First Principles. *Nanomaterials* **2023**, *13*, 1519. <https://doi.org/10.3390/nano13091519>

Academic Editor: Gyaneshwar P. Srivastava

Received: 16 April 2023

Revised: 26 April 2023

Accepted: 27 April 2023

Published: 29 April 2023



Copyright: © 2023 by the authors. Licensee MDPI, Basel, Switzerland. This article is an open access article distributed under the terms and conditions of the Creative Commons Attribution (CC BY) license (<https://creativecommons.org/licenses/by/4.0/>).

1. Introduction

The world's energy demand is increasing due to the development of science and technology. Thermoelectric modules can directly convert electricity into thermal energy for cooling and heating and can also harvest waste heat for electrical power. They have, thus, attracted significant attention [1,2]. The performance of thermoelectric materials is usually evaluated by the dimensionless figure of merit (*ZT*), which is defined as $ZT = S^2\sigma T / (\kappa_e + \kappa_l)$, where *S* is the Seebeck coefficient, σ is the electrical conductivity, *T* is the absolute temperature, and κ_e and κ_l are the electronic thermal conductivity and the lattice thermal conductivity, respectively [3,4]. The higher the *ZT* value, the better the efficiency μ of the thermoelectric conversion. The efficiency of thermoelectric devices can reach 25% in power generation and exceed traditional refrigeration when $ZT > 3$ [5,6]. The definition of *ZT* suggests that high-performance thermoelectric devices depend on the increase in the power factor $PF = S^2\sigma$ ($\text{W}\cdot\text{m}^{-1} \text{K}^{-2}$) and the decrease in thermal conductivity.

However, due to the Wiedemann–Franz law, there is a coupling relationship between electronic transport coefficients, which makes it a significant challenge to improve *ZT* and enhance thermoelectric performance [7]. In inorganic thermoelectric materials, the improvement of the *ZT* value is a slow process until the paradigm of “phonon glass, electronic crystal” was first proposed by Slack et al. [8]. This paradigm indicates that we need to maintain the electrical conductance at a high level to maximize the *ZT* value while trying to reduce the thermal conductance. Subsequently, in order to improve thermoelectric performance, many advanced methods have been proposed, which can be divided into two main categories, namely, phonon engineering and electronic engineering, for optimizing phonon and electronic transport properties, respectively [5,9–14]. Phonon engineering is focused on the modulation of lattice thermal conductivity by suppressing the mean free

path of phonons. Electron engineering aims at the modulation of the power factor and Seebeck coefficient under the optimum carrier concentration. This includes strain engineering [15–20], doping defects [21–23], molecular junction [4,24–26], superlattices [27–29], and heterostructures [30,31].

Two-dimensional materials with layered structures have attracted extensive attention as efficient thermoelectric materials due to their outstanding electronic and mechanical properties [32,33]. In addition, 2D materials exhibit great potential as thermoelectric candidates due to the enhanced Seebeck coefficient resulting from the increased density of states in proximity to the Fermi energy level [34,35]. In the past several decades, the thermoelectric performance of a series of 2D materials has been theoretically predicted and samples have been experimentally fabricated [36–38]. In particular, many group VI compounds, such as single layers of transition metal dichalcogenides (TMDCs), MX_2 ($M = Mo, W, Ti$, and $X = S, Se, Te$), and group IV metal chalcogenides, AX_2 ($A = Ge, Sn, Pb$, and $X = S, Se, Te$), have attracted attention in recent decades due to their unique semiconducting characteristics [35,39,40]. Recently, a novel class of 2D group IV metal chalcogenides, $(AX)_2$ ($A = Si, Ge, Sn, Pb$; $X = Se, Te$), has been theoretically predicted through ab initio calculations [41]. Dong et al. reported that the γ -SnX ($X = S, Se, or Te$) has high thermoelectric performance due to the low thermal conductivity [14]. Then, Jia et al. reported high thermoelectric properties due to strong anharmonic effects in the $(PbX)_2$ ($X = S, Se, Te$) monolayer [42]. Thus, the γ -phase group IV metal chalcogenides exhibit great potential as candidates for thermoelectric applications.

In this work, we predicted a series of 2D γ -phase group IV metal chalcogenides, namely, γ -PbSnX₂ ($X = S, Se, Te$), based on the crystal structure of γ -AX ($A = Pb, Sn$ and $X = S, Se, Te$). In addition, we investigated the thermoelectric transport properties using first-principles calculations combined with the Boltzmann transport equation. The density functional theory (DFT) has been widely used to predict the thermoelectric properties of materials [43,44]. The results show that these materials have high power factors and low lattice thermal conductivity, leading to a high figure of merit (ZT). The studies indicate that these materials are potential candidates for high-temperature thermoelectric materials.

2. Computational Method

In this work, we performed first-principles simulations using the Vienna Ab initio Simulation Package (VASP) based on density functional theory (DFT) [45,46] and using the projector augmented wave (PAW) pseudopotential [47–50]. The generalized gradient approximation (GGA) method with the Perdew–Burke–Ernzerhof (PBE) exchange–correlation (XC) functional was employed [51]. The total energy convergence criterion of 10^{-8} eV, the force convergence criterion of 0.001 eV/Å, and the kinetic energy cutoff of 500 eV were used to optimize the crystals [50]. A set of $15 \times 15 \times 1$ Monkhorst-Pack k-points [52] was used to sample the Brillouin zone. A 20 Å vacuum layer was set in the direction of the z-axis to avoid the interaction of periodic layers along the z-axis and the DFT-D3 method was used to correct the van der Waals (VDW) interactions [53]. A hybrid functional (HSE06) was used to calculate the electronic band properties of materials. The thermoelectric transport coefficient was calculated by solving the Boltzmann transport equation with the BoltzTraP package [54]. The relaxation time was calculated using the deformation potential theory and effective mass approximation. A $3 \times 3 \times 1$ supercell was used to calculate the second-order and third-order force constants of the materials through the finite displacement method. The cutoff radius of the third-order force constant was set as the sixth-nearest neighbors. Lattice thermal conductivity was obtained by solving the Boltzmann transport equation using ShengBTE, and a grid density of $60 \times 60 \times 1$ k-points was used to ensure convergence [55].

3. Results

3.1. Structure and Stability

The monolayer γ -PbSnX₂ (X = S, Se, Te) can be constructed from a γ -AX (A = Pb, Sn and X = S, Se, Te) monolayer by replacing one layer of chalcogen Pb/Sn atoms with another layer of chalcogen Sn/Pb atoms in the middle side, resulting in a hexagonal lattice structure with a $P3m1$ space group (Figures 1 and S1). The calculated lattice constants of γ -PbSnS₂, γ -PbSnSe₂, and γ -PbSnTe₂ are $a = b = 3.96$ Å, 4.11 Å, and 4.37 Å, respectively. The specific crystal structure parameters are shown in Table 1.

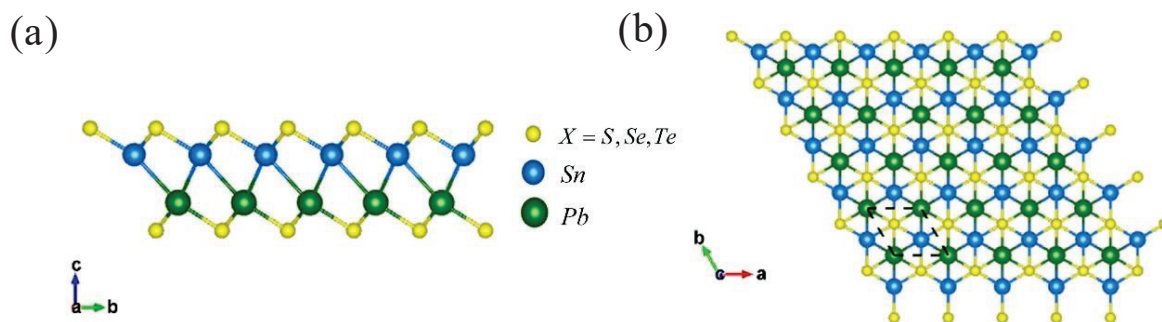


Figure 1. (a) Side view and (b) top view of the optimized γ -PbSnX₂ (X = S, Se, Te) monolayer structure.

Table 1. Structural parameters for the γ -PbSnX₂ (X = S, Se, Te). Here, a is the lattice constant, d_{Sn-X} , d_{Pb-X} , and d_{Pb-Sn} are the Sn-X, Pb-X, and Pb-Sn bond lengths, respectively, and h is the vertical distance between the two outermost X atoms in Angstroms, as shown in Figure 1.

Material	a (Å)	d_{Sn-X} (Å)	d_{Pb-X} (Å)	d_{Pb-Sn} (Å)	h (Å)	C_{11} (N/m)	C_{12} (N/m)	C_{66} (N/m)
PbSnS ₂	3.96	2.64	2.68	3.58	5.49	39.5	12.9	13.2
PbSnSe ₂	4.11	2.77	2.81	3.51	5.52	42.7	14.5	14.1
PbSnTe ₂	4.37	2.97	3.01	3.46	5.59	43.5	12.7	15.4

We next verified the structural stability of the γ -PbSnX₂ (X = S, Se, Te) monolayer, including the mechanical, dynamic, and thermal stabilities. For the mechanical stability, we used the Born criterion of 2D materials as $C_{11} > |C_{12}| > 0$ and $C_{66} > 0$ [56]. The calculated elastic constants of γ -PbSnS₂, γ -PbSnSe₂, and γ -PbSnTe₂ were $C_{11} = 39.5$, 42.7 and 43.5 N/m, $C_{12} = 12.9$, 14.5 , and 12.7 N/m, and $C_{66} = 13.2$, 14.1 , and 15.4 N/m, respectively (Figure S2). These calculated values are given in Table 1 and satisfy the Born criterion. For the dynamic stability, we calculated the phonon dispersion of γ -PbSnX₂. Figure 2a–c shows the phonon dispersion curve of γ -PbSnX₂. Each unit cell of the γ -PbSnX₂ monolayer has four atoms, with three acoustic and nine optical branches. The phonon frequencies of the γ -PbSnX₂ monolayer are all positive, indicating the dynamic stability of the γ -PbSnX₂ monolayer. They all have very low phonon frequencies and lead to a decrease in their phonon frequencies as the atomic mass of sulfur group elements increases. More interestingly, an apparent coupling occurs between optical and acoustic phonon modes in γ -PbSnX₂ monolayers, which might lead to a low lattice thermal conductivity because of anharmonic scattering. To determine the thermal stability, we used ab initio molecular dynamics (AIMD) simulations to determine the stability of γ -PbSnX₂ at 900 K. A $4 \times 4 \times 1$ supercell was used for the AIMD simulation. The AIMD simulation results are shown in Figure 2d–f. The total energy was almost unchanged at a temperature of 900 K for 10 ps. In addition, the structure exhibited no obvious deformation at 900 K. The results confirm the thermal stability of γ -PbSnX₂ at 900 K. In addition, we also calculated the formation enthalpy (ΔH) through:

$$\Delta H = \frac{H_{PbSnX_2} - H_{Pb} - H_{Sn} - 2H_X}{4} \quad (1)$$

where H_{PbSnX_2} is the total energy of the γ -PbSnX₂ monolayer, H_{Pb} , H_{Sn} , and H_X are the energy of a single atom (Pb, Sn, and X = S, Se, Te) of the structure.

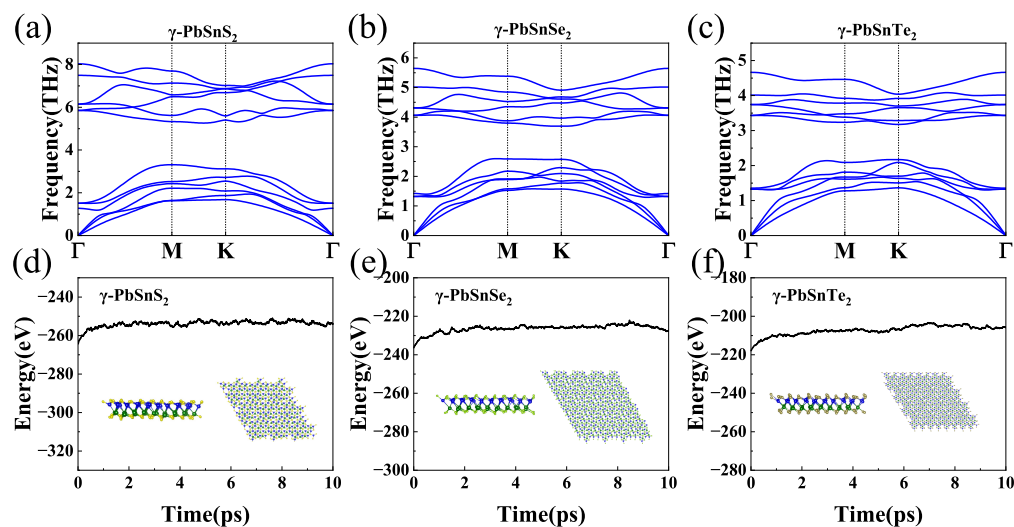


Figure 2. (a–c) Phonon dispersions for γ -PbSnX₂ (X = S, Se, Te). (d–f) Total potential energy fluctuation and structures in AIMD simulations of γ -PbSnX₂ (X = S, Se, Te).

According to Equation (1), it is obvious that negative formation energies are related exothermic chemical reactions, which imply stable products. As listed in Table S1 (in the Supplementary Material), the formation enthalpy values of γ -PbSnS₂, γ -PbSnSe₂, and γ -PbSnTe₂ are -0.45 , -0.37 , and -0.23 eV/atom, respectively, which indicates that all the monolayers are stable. In addition, it can be seen from Table S1 that the lighter structures of atoms are more stable because they are more likely to form through exothermic reactions.

In conclusion, we determined the stability of materials by calculating their formation enthalpy, mechanical stability, dynamic stability, and thermal stability. The formation enthalpy of the material calculated using Equation (1) is negative, which indicates that the material can release energy during chemical formation and reach a stable state. The phonon dispersion curve can reflect the dynamic stability of the structure, indicating that the material is dynamically stable. The AIMD simulation results can reflect the thermal stability of the structure at 900K, indicating that the structure can exist stably at 900 K. These results indicate that these structures are stable.

3.2. Electronic Band Structure

Figure 3 shows the electronic band structures of the γ -PbSnX₂ (X = S, Se, Te) monolayers calculated using the PBE and HSE06 exchange–correlation functionals. The corresponding band gap values are given in Table 2. They are both indirect band gaps with a conduction band minimum (CBM) at the high symmetry point Γ (0, 0, 0) and a valence band maximum (VBM) between the high symmetry points Γ (0,0,0) and K (1/3, 1/3, 0). The band gap calculated using HSE06 is larger than that calculated using PBE. It is noted that the PBE functional often underestimated the band gap value, while the HSE functional gave a reliable band gap value compared with the experiment. The band gaps of γ -PbSnS₂, γ -PbSnSe₂, and γ -PbSnTe₂ were 0.86 (1.37) eV, 0.63 (1.08) eV and 0.61 (0.98) eV, respectively. The band gaps calculated by all the methods gradually decreased as the atomic number of the substituted chalcogenide element (S, Se, and Te) increased. The thermoelectric characteristics of the γ -PbSnX₂ monolayer can be easily tuned at a suitable doping concentration for 2D materials, according to such a moderate band gap. The band types and shapes calculated using the PBE and HSE functionals were essentially unchanged except for the band gap. The variable situation theory and effective mass approximation method were used to calculate the carrier mobility and relaxation time of the material, and the band values near the VBM and CBM were used for fitting. However, the band structure and

shape calculated using the PBE and HSE06 functionals in the VBM and CBM were the same; only the band gap was different. This means that the dispersion relationship between the PBE and HSE functionals was consistent and the effective mass calculated using the PBE and HSE06 functionals was assumed to be the same. Therefore, we used the PBE function to obtain the effective mass and carrier mobility of these materials. The partial density of states (PDOS) of the γ -PbSnX₂ is shown in Figure 3d–f, with the valence bands closer to the Fermi energy level. The valence bands around the Fermi level originate from the S, Se, and Te atoms, and the conduction bands are jointly contributed by Sn or Pb, S, Se, and Te atoms. Figure 3d–f show that γ -PbSnS₂, γ -PbSnSe₂, and γ -PbSnTe₂ all have a very sharp density of state peaks at the Fermi level attachment, where γ -PbSnS₂ has a higher density of state peaks than γ -PbSnSe₂ and γ -PbSnTe₂.

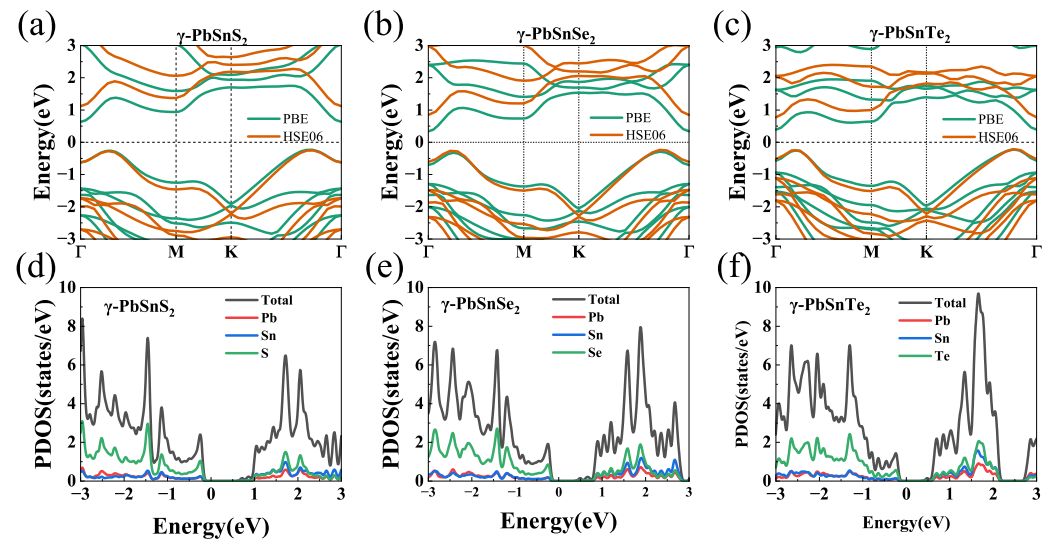


Figure 3. (a–c) Band structures of γ -PbSnX₂ (X = S, Se, Te) calculated using the PBE and HSE06 functionals. (d–f) Partial density of states (PDOS) of the γ -PbSnX₂. The Fermi level was set as zero.

Table 2. Bandgap of γ -PbSnX₂ (X = S, Se, Te) calculated using PBE and HSE06.

Material	Structure	Gap-Type	E _g (PBE)	E _g (HSE06)
PbSnS ₂	hexagonal (2D)	Indirect	0.86 eV	1.37 eV
PbSnSe ₂	hexagonal (2D)	Indirect	0.63 eV	1.08 eV
PbSnTe ₂	hexagonal (2D)	Indirect	0.61 eV	0.98 eV

3.3. Carrier Mobility and Relaxation Time

We estimated the electrical characteristics of the γ -PbSnX₂ (X = S, Se, Te) monolayer using the BoltzTraP package, which is based on the semi-classical Boltzmann transport equation. Additionally, the BoltzTraP2 package uses constant relaxation time approximation, which means the calculated results are divided by the relaxation time. Therefore, in order to accurately calculate the thermoelectric properties of the material, the relaxation time of the material must be obtained.

Here, the carrier mobilities and relaxation time of the 2D materials are calculated using deformation potential theory and the effective mass approximation method [57–59]:

$$\mu_{2D} = \frac{e\hbar^3 C_{2D}}{k_B T |m^*|^2 E_1^2} \quad (2)$$

$$\tau = \frac{\hbar^3 C_{2D}}{k_B T |m^*|^2 E_1^2} \quad (3)$$

where \hbar is the reduced Planck constant, k_B is the Boltzmann constant, T is the temperature, μ_{2D} is the carrier mobility, and τ is the relaxation time. C_{2D} is the elastic constant defined by $C_{2D} = \frac{\partial^2 E_{total}/\partial \epsilon^2}{S_0}$, where E_{total} is the total energy after applying a uniaxial term ($\epsilon = \Delta l/l_0$), and S_0 is the area at equilibrium. m^* is the effective mass defined by $m^* = \hbar^2 \left(\frac{d^2 \epsilon(k)}{dk^2} \right)^{-1}$; we calculated the effective mass using vaspkit code [60]. Six discrete points were selected in the CBM and VBM attachments for polynomial fitting, and the truncation radius was 0.015/Å to 0.01/Å. With the decrease in the truncation radius, Δk also decreased, but the results of the effective mass calculation were almost constant. Therefore, we believe that the results converged, that is, smaller Δk values would not have changed the reported effective mass. E_1 is the deformation potential constants defined by $E_d = \Delta E/\Delta \epsilon$, where ΔE is the energy shift of the band edge of CBM or VBM with respect to the vacuum level (Figure S3).

Table 3 shows the results of the electric and hole carrier mobilities calculated with the theory of deformation potential at 300 K. Among them, γ -PbSnS₂ and γ -PbSnSe₂ had a ultra-high hole carrier mobility; in particular, γ -PbSnS₂ had the highest hole mobility of $4.04 \times 10^3 \text{ cm}^2 \text{ V}^{-1} \text{ s}^{-1}$, which was significantly higher than that of other two-dimensional semiconductors, e.g., MoS₂ ($285 \text{ cm}^2 \text{ V}^{-1} \text{ s}^{-1}$) [61], SnS₂ ($756 \text{ cm}^2 \text{ V}^{-1} \text{ s}^{-1}$) [62], SnSe₂ ($462 \text{ cm}^2 \text{ V}^{-1} \text{ s}^{-1}$) [62], γ -PbX₂ ($780 \text{ cm}^2 \text{ V}^{-1} \text{ s}^{-1}$) [42], and γ -SnX₂ ($1364 \text{ cm}^2 \text{ V}^{-1} \text{ s}^{-1}$) [14]. The high carrier mobility of γ -PbSnS₂ and γ -PbSnSe₂ was due to a combination of a low effective mass and deformation potential energy. The high hole carrier mobility indicates that γ -PbSnS₂ and γ -PbSnSe₂ are potential p-type semiconductors. In addition, Hung et al. showed that a high carrier mobility is one of the important parameters for screening thermoelectric materials [63,64]. The ultra-high carrier mobility indicates that γ -PbSnX₂ has excellent hole transport properties and is an excellent thermoelectric material.

Table 3. Calculated effective mass (m^*), elastic constant (C_{2D}), deformation potential (E_1), carrier mobility (μ_{2D}), and relaxation time (τ) for electrons (e) and holes (h) in the γ -PbSnX₂ monolayer at 300 K.

Material	Carrier	C_{2D} (N/m)	m^*/m_0	E_1 (eV)	μ_{2D} ($\times 10^3 \text{ cm}^2 \text{ V}^{-1} \text{ s}^{-1}$)	τ (ps)
PbSnS ₂	e	39.5	0.22	4.92	0.476	0.059
	h		0.50	1.02	4.04	1.14
PbSnSe ₂	e	42.75	0.18	5.52	0.654	0.067
	h		0.357	2.66	1.421	0.288
PbSnTe ₂	e	43.55	0.23	6.52	0.256	0.033
	h		0.596	4.14	0.245	0.083

3.4. Thermoelectric Properties

We investigated the thermoelectric properties of the materials in the temperature range of 300 K to 900 K. As shown in Figure 4a–c, all three materials had a high Seebeck coefficient at 300 K. Among them, the Seebeck coefficients of γ -PbSnS₂, γ -PbSnSe₂, and γ -PbSnTe₂ were 1400 $\mu\text{V}/\text{K}$, 800 $\mu\text{V}/\text{K}$, and 900 $\mu\text{V}/\text{K}$, respectively, which were much higher than those of other common 2D materials, such as SnTe (600 $\mu\text{V}/\text{K}$) [65], MoSe₂ (427 $\mu\text{V}/\text{K}$) [66], and WS₂ (328 $\mu\text{V}/\text{K}$) [67]. The Seebeck coefficient of γ -PbSnS₂ was higher than those of γ -PbSnSe₂ and γ -PbSnTe₂. This is because γ -PbSnS₂ has a higher density of state peaks than γ -PbSnSe₂ and γ -PbSnTe₂ near the Fermi energy level (as shown in Figure 3), and the Seebeck coefficient is proportional to the density of state peaks: $S \propto d(\text{DOS})/dE$. The high density of state peaks near the Fermi energy level indicates that the material will have a higher Seebeck coefficient. The high Seebeck coefficient indicates that these materials may have high thermoelectric properties.

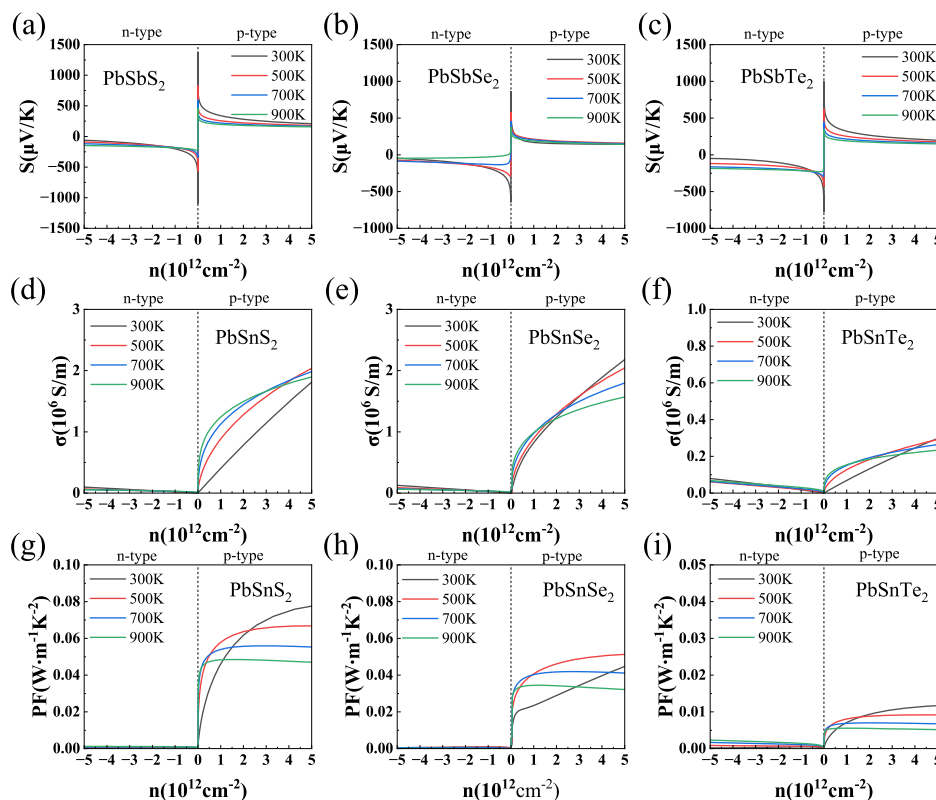


Figure 4. (a–c) Seebeck coefficients, (d–f) electrical conductivity, and (g–i) power factor (PF) of γ - $PbSnX_2$ ($X = S, Se, Te$) as a function of carrier concentration.

Figure 4d–f show the electrical conductivities σ obtained by multiplying σ/τ by τ , where σ/τ was calculated using the BoltzTraP package and τ is the relaxation time calculated using deformation potential theory. The electrical conductivity of γ - $PbSnX_2$ ($X = S, Se, Te$) exhibited a similar behavior at different temperatures and decreased as the temperature increased. This was caused by the enhanced lattice vibrations and electron scattering at high temperature. The electric conductivity of γ - $PbSnX_2$ gradually decreased as the atomic number of the substituted chalcogenide element (S, Se, and Te) increased. In addition, the value of the conductivity is related to the carrier concentration. The conductivity of γ - $PbSnX_2$ was higher in the positive carrier concentration range, which shows the characteristics of p-type semiconductors. It is worth noting that the electrical conductivity of γ - $PbSnX_2$ reached the same order (10^6 – 10^7 / Ωm) as that of metals due to its ultra-high carrier mobility. The high Seebeck coefficient and conductivity indicate that they have a high power factor ($PF = S^2\sigma$), which is important for thermoelectric devices. With the Seebeck coefficient and electrical conductivity, we evaluated the power factor (PF) of γ - $PbSnX_2$ ($X = S, Se, Te$), as shown in Figure 4g–i. All three materials produced the same trend for the power factor, which decreased with the increase in temperature. The γ - $PbSnS_2$ had the highest PF because of its higher Seebeck coefficient and electrical conductivity. Moreover, the PF values of these materials were maximum in the negative range due to their p-type properties. The PF is one of the important factors in evaluating the performance of thermoelectric materials, so a high PF predicts that the material will have high thermoelectric properties.

Materials with high thermoelectric properties require low thermal conductivity in addition to a high power factor. Figure 5 shows the phonon transport properties of γ - $PbSnX_2$ ($X = S, Se, Te$). The results show that both γ - $PbSnX_2$ have a very low thermal conductivity, which is about 6–8 W/mK at room temperature, and the value of the lattice thermal conductivity decreased with increasing temperature. In order to understand the

lattice thermal conductivity of the γ -PbSnX₂ monolayer, we explored the phonon-related properties, such as the phonon group velocity and anharmonic scattering rates. As shown in Figure 5a–c, the three acoustic phonon branches (ZA/TA/LA) become entangled and strong coupling occurs between the optical and acoustic phonon modes, which can strengthen the phonon scattering mechanism and, thus, lower κ_l . Figure 5d–f show the phonon group velocities of γ -PbSnX₂, and it can be seen that they are both low, and low group velocities can lead to a low lattice thermal conductivity. The inverse of the phonon relaxation time in the relaxation time approximation (RTA) is equal to the total scattering rate, which is the sum of the isotopic scattering rate (τ_i^{-1}), the boundary scattering rate (τ_b^{-1}), and the anharmonic scattering rate (τ_a^{-1}). In general, a higher value indicates stronger phonon–phonon scattering and a lower phonon relaxation time, which is beneficial for reducing the lattice thermal conductivity. As shown in Figure 5g–i, the γ -PbSnX₂ monolayer exhibited high phonon–phonon scattering rates (anharmonic scattering rates) and they are relatively close to each other. In addition, the value of the lattice thermal conductivity increased with the atomic number of the elements (S, Se, and Te), which is mainly due to the increase in the atomic mass and the decrease in the phonon frequency. In conclusion, the strong coupling between phonons, lower phonon group velocities, and higher scattering rates lead to lower lattice thermal conductivity, indicating that γ -PbSnX₂ may be a suitable thermoelectric material.

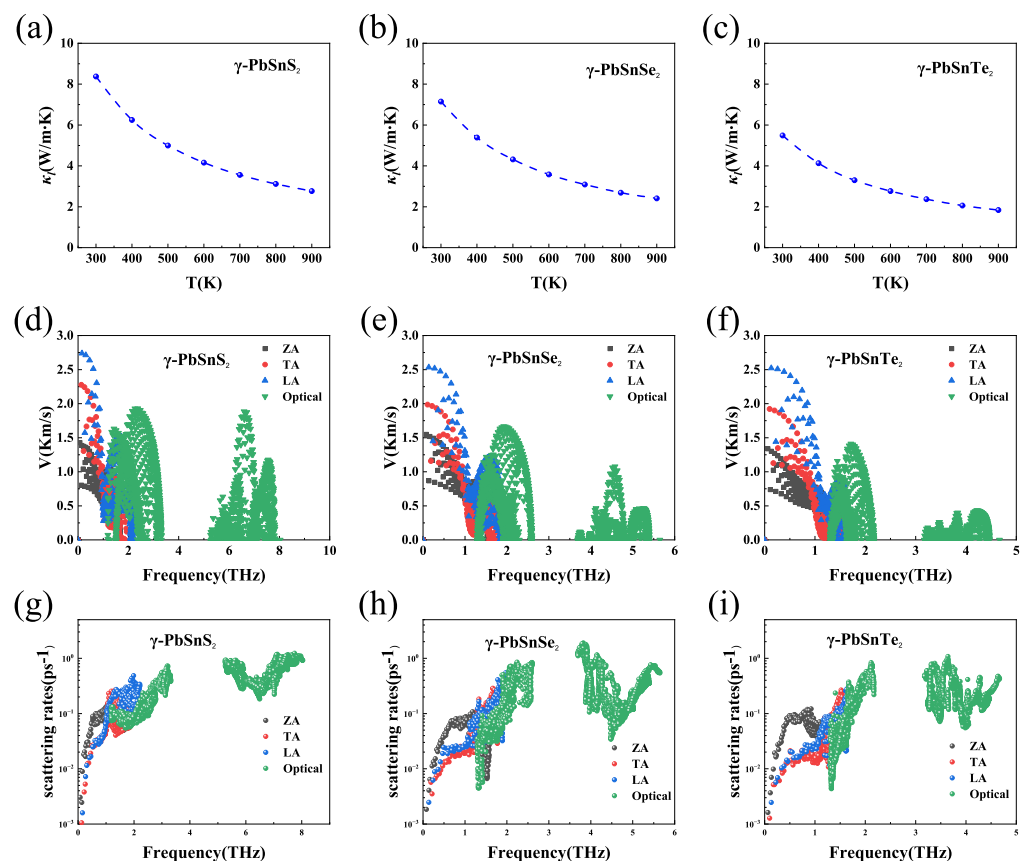


Figure 5. (a–c) Lattice thermal conductivity at different temperatures, (d–f) phonon group velocity at 300 K, and (g–i) anharmonic scattering rates at 300 K of γ -PbSnX₂ (X = S, Se, Te).

After all transport coefficients were obtained, the dependence of ZT on the carrier concentration of the γ -PbSnX₂ monolayer at different temperatures was calculated, as shown in Figure 6. All γ -PbSnX₂ monolayers exhibited the maximum thermoelectric properties in the positive carrier concentration range due to their higher hole mobility. The ZT values for all three materials showed the same trend: increasing with increasing temperature. Among them, the ZT value of γ -PbSnTe₂ was lower, reaching a maximum of only 1.4 at

900 K, which is due to its low power factor. In addition, γ -PbSnS₂ and γ -PbSnSe₂ reached ultra-high *ZT* values of 2.65 and 2.96 at 900 K due to a combination of their low lattice thermal conductivity and high power factor. These ultra-high *ZT* values for γ -PbSnX₂ contribute to their low thermal conductivity along with their high power factor. High *ZT* values indicate that γ -PbSnS₂ and γ -PbSnSe₂ are high temperature thermoelectric materials with a good performance.

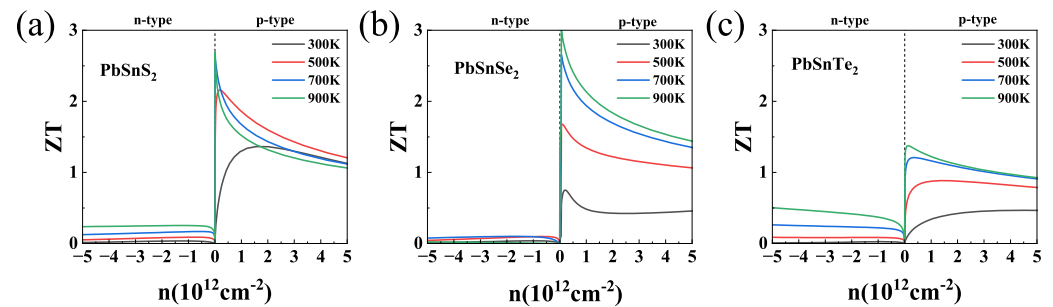


Figure 6. (a–c) The *ZT* values of γ -PbSnX₂ (*X* = S, Se, Te) as a function of carrier concentration at 300 K.

4. Conclusions

In this study, we constructed a series of γ -PbSnX₂ (*X* = S, Se, Te) 2D monolayer material based on γ -(AX)₂ (*A* = Sn, Pb and *X* = S, Se, Te) and calculated their thermoelectric properties using Boltzmann transport theory combined with first principles. The results show that these materials are narrow bandgap semiconductors with bandgap values of 0.98–1.37 eV according to the HSE06 functional. They have high hole carrier mobilities; in particular, γ -PbSnS₂ has a hole carrier mobility of $4.04 \times 10^3 \text{ cm}^2 \text{ V}^{-1} \text{ s}^{-1}$. In addition, they all have high Seebeck coefficients and intrinsically low lattice thermal conductivities, which are 800–1400 $\mu\text{V/K}$ and 6–8 W/mK at temperatures of 300 K. The *ZT* values of γ -PbSnS₂, γ -PbSnSe₂, and γ -PbSnTe₂ at 900K were 2.65, 2.96, and 1.36, respectively. This high thermoelectric performance indicates that γ -PbSnX₂ monolayer materials are excellent thermoelectric materials. Our theoretical study may help to optimize the thermoelectric properties of such materials.

Supplementary Materials: The following supporting information can be downloaded at: <https://www.mdpi.com/article/10.3390/nano13091519/s1>, Figure S1: The structure of γ -PbSnX₂ (*X* = S, Se, Te) and its possible synthesis process; Figure S2: The energy-strain relationship of γ -PbSnX₂ (*X* = S, Se, Te); Figure S3: Calculated band energies of the CBM and VBM of γ -PbSnX₂ (*X* = S, Se, Te) with respect to the vacuum energy as a function of uniaxial strains. The red solid lines are linear fitting curves. The fitted slopes are presented, which correspond to the DP; Table S1: The energy of γ -PbSnX₂ monolayer and a single atom (Pb, Sn and *X* = S, Se, Te) of structure, and the formation enthalpy (ΔH) of γ -PbSnX₂ monolayer.

Author Contributions: Conceptualization, C.D. and Z.D.; methodology, C.D.; software, C.D. and Z.D.; validation, N.L., J.Z., L.T., W.R. and K.C.; investigation, C.D. and Z.D.; resources, K.C.; data curation, C.D.; writing—original draft preparation, C.D.; writing—review and editing, K.C.; project administration, K.C.; funding acquisition, K.C. and W.R. All authors have read and agreed to the published version of the manuscript.

Funding: This work was supported by the National Natural Science Foundation of China (Grant No. 11974106 and 12204163) and the Natural Science Foundation of Hunan Province of China (Grant No. 2022JJ40032).

Data Availability Statement: Not applicable.

Conflicts of Interest: The authors declare no conflict of interest.

References

1. Yang, L.; Chen, Z.G.; Dargusch, M.S.; Zou, J. High Performance Thermoelectric Materials: Progress and Their Applications. *Adv. Energy Mater.* **2018**, *8*, 1701797. [[CrossRef](#)]
2. Chu, S.; Majumdar, A. Opportunities and challenges for a sustainable energy future. *Nature* **2012**, *488*, 294–303. [[CrossRef](#)] [[PubMed](#)]
3. Huang, H.H.; Fan, X.; Singh, D.J.; Zheng, W.T. Thermoelectric properties of monolayer GeAsSe and SnSbTe. *J. Mater. Chem. C* **2020**, *8*, 9763–9774. [[CrossRef](#)]
4. Wu, D.; Cao, X.H.; Chen, S.Z.; Tang, L.M.; Feng, Y.X.; Chen, K.Q.; Zhou, W.X. Pure spin current generated in thermally driven molecular magnetic junctions: A promising mechanism for thermoelectric conversion. *J. Mater. Chem. A* **2019**, *7*, 19037–19044. [[CrossRef](#)]
5. Zeng, Y.J.; Wu, D.; Cao, X.H.; Zhou, W.X.; Tang, L.M.; Chen, K.Q. Nanoscale Organic Thermoelectric Materials: Measurement, Theoretical Models, and Optimization Strategies. *Adv. Funct. Mater.* **2020**, *30*, 1903873. [[CrossRef](#)]
6. Zhang, X.; Zhao, L.D. Thermoelectric materials: Energy conversion between heat and electricity. *J. Mater.* **2015**, *1*, 92–105. [[CrossRef](#)]
7. Jonson, M.; Mahan, G.D. Mott's formula for the thermopower and the Wiedemann-Franz law. *Phys. Rev. B* **1980**, *21*, 4223–4229. [[CrossRef](#)]
8. Slack, G.A.; Rowe, D. *CRC Handbook of Thermoelectrics*; CRC Press: Boca Raton, FL, USA, 1995.
9. Ding, Z.K.; Zeng, Y.J.; Pan, H.; Luo, N.; Zeng, J.; Tang, L.M.; Chen, K.Q. Edge states of topological acoustic phonons in graphene zigzag nanoribbons. *Phys. Rev. B* **2022**, *106*, L121401. [[CrossRef](#)]
10. Pan, H.; Ding, Z.K.; Zeng, B.W.; Luo, N.N.; Zeng, J.; Tang, L.M.; Chen, K.Q. Ab initio Boltzmann approach to coupled magnon-phonon thermal transport in ferromagnetic crystals. *Phys. Rev. B* **2023**, *107*, 104303. [[CrossRef](#)]
11. Pan, H.; Ding, Z.K.; Zeng, Y.J.; Li, Q.Q.; Tang, L.M.; Chen, K.Q. Tuning quantum heat transport in magnetic nanostructures by spin-phonon interaction. *Europhys. Lett.* **2022**, *138*, 36001. [[CrossRef](#)]
12. Pan, H.; Tang, L.M.; Chen, K.Q. Quantum mechanical modeling of magnon-phonon scattering heat transport across three-dimensional ferromagnetic/nonmagnetic interfaces. *Phys. Rev. B* **2022**, *105*, 064401. [[CrossRef](#)]
13. Zeng, B.; Ding, Z.K.; Pan, H.; Luo, N.; Zeng, J.; Tang, L.M.; Chen, K.Q. Strong strain-dependent phonon hydrodynamic window in bilayer graphene. *Appl. Phys. Lett.* **2022**, *121*, 252202. [[CrossRef](#)]
14. Dong, B.; Wang, Z.; Hung, N.T.; Oganov, A.R.; Yang, T.; Saito, R.; Zhang, Z. New two-dimensional phase of tin chalcogenides: Candidates for high-performance thermoelectric materials. *Phys. Rev. Mater.* **2019**, *3*, 013405. [[CrossRef](#)]
15. Guo, S.D. Biaxial strain tuned thermoelectric properties in monolayer PtSe₂. *J. Mater. Chem. C* **2016**, *4*, 9366–9374. [[CrossRef](#)]
16. Lin, C.M.; Chen, W.C.; Chen, C.C. First-principles study of strain effect on the thermoelectric properties of LaP and LaAs. *Phys. Chem. Chem. Phys.* **2021**, *23*, 18189–18196. [[CrossRef](#)]
17. Miao, T.; Yu, D.; Xing, L.; Li, D.; Jiao, L.; Ma, W.; Zhang, X. Current Rectification in a Structure: ReSe₂/Au Contacts on Both Sides of ReSe₂. *Nanoscale Res. Lett.* **2019**, *14*, 1. [[CrossRef](#)]
18. Wu, C.W.; Ren, X.; Xie, G.; Zhou, W.X.; Zhang, G.; Chen, K.Q. Enhanced High-Temperature Thermoelectric Performance by Strain Engineering in BiOCl. *Phys. Rev. Appl.* **2022**, *18*, 014053. [[CrossRef](#)]
19. Wu, Y.; Chen, Z.; Nan, P.; Xiong, F.; Lin, S.; Zhang, X.; Chen, Y.; Chen, L.; Ge, B.; Pei, Y. Lattice Strain Advances Thermoelectrics. *Joule* **2019**, *3*, 1276–1288. [[CrossRef](#)]
20. Zhou, W.X.; Wu, D.; Xie, G.; Chen, K.Q.; Zhang, G. α -Ag₂S: A Ductile Thermoelectric Material with High ZT. *ACS Omega* **2020**, *5*, 5796–5804. [[CrossRef](#)]
21. Gu, B.C.; Li, Z.; Liu, J.D.; Zhang, H.J.; Ye, B.J. Effect of vacancies on thermoelectric properties of β -CuAgSe studied by positron annihilation. *Appl. Phys. Lett.* **2019**, *115*, 192106. [[CrossRef](#)]
22. Han, D.; Yang, X.; Du, M.; Xin, G.; Zhang, J.; Wang, X.; Cheng, L. Improved thermoelectric properties of WS₂-WSe₂ phononic crystals: insights from first-principles calculations. *Nanoscale* **2021**, *13*, 7176–7192. [[CrossRef](#)] [[PubMed](#)]
23. Xie, Z.X.; Chen, X.K.; Yu, X.; Deng, Y.X.; Zhang, Y.; Zhou, W.X.; Jia, P.Z. Intrinsic thermoelectric properties in biphenylene nanoribbons and effect of lattice defects. *Comput. Mater. Sci.* **2023**, *220*, 112041. [[CrossRef](#)]
24. Cao, X.H.; Wu, D.; Feng, Y.X.; Zhou, W.X.; Tang, L.M.; Chen, K.Q. Effect of electrophilic substitution and destructive quantum interference on the thermoelectric performance in molecular devices. *J. Phys. Condens. Matter* **2019**, *31*, 345303. [[CrossRef](#)] [[PubMed](#)]
25. Deng, Y.X.; Chen, S.Z.; Hong, J.; Jia, P.Z.; Zhang, Y.; Yu, X.; Chen, K.Q. Perfect spin-filtering effect in molecular junctions based on half-metallic penta-hexa-graphene nanoribbons. *J. Phys. Condens. Matter* **2022**, *34*, 285302. [[CrossRef](#)] [[PubMed](#)]
26. Zeng, Y.J.; Wu, D.; Cao, X.H.; Feng, Y.X.; Tang, L.M.; Chen, K.Q. Significantly enhanced thermoelectric performance of molecular junctions by the twist angle dependent phonon interference effect. *J. Mater. Chem. A* **2020**, *8*, 11884–11891. [[CrossRef](#)]
27. Gibson, Q.D.; Zhao, T.; Daniels, L.M.; Walker, H.C.; Daou, R.; Hebert, S.; Zanella, M.; Dyer, M.S.; Claridge, J.B.; Slater, B.; et al. Low thermal conductivity in a modular inorganic material with bonding anisotropy and mismatch. *Science* **2021**, *373*, 1017–1022. [[CrossRef](#)]
28. Wang, J.; Cao, X.H.; Zeng, Y.J.; Luo, N.N.; Tang, L.M.; Chen, K.Q. Excellent thermoelectric properties of monolayer MoS₂-MoSe₂ aperiodic superlattices. *Appl. Surf. Sci.* **2023**, *612*, 155914. [[CrossRef](#)]

29. Xie, Z.X.; Zhang, Y.; Yu, X.; Li, K.M.; Chen, Q. Ballistic thermal conductance by phonons through superlattice quantum-waveguides. *J. Appl. Phys.* **2014**, *115*, 104309. [[CrossRef](#)]
30. Jia, P.Z.; Xie, J.P.; Chen, X.K.; Zhang, Y.; Yu, X.; Zeng, Y.J.; Xie, Z.X.; Deng, Y.X.; Zhou, W.X. Recent progress of two-dimensional heterostructures for thermoelectric applications. *J. Phys. Condens. Matter* **2023**, *35*, 073001. [[CrossRef](#)]
31. Jia, P.Z.; Zeng, Y.J.; Wu, D.; Pan, H.; Cao, X.H.; Zhou, W.X.; Xie, Z.X.; Zhang, J.X.; Chen, K.Q. Excellent thermoelectric performance induced by interface effect in MoS₂/MoSe₂ van der Waals heterostructure. *J. Phys. Condens. Matter* **2020**, *32*, 055302. [[CrossRef](#)]
32. Zhang, G.; Zhang, Y.W. Thermoelectric properties of two-dimensional transition metal dichalcogenides. *J. Mater. Chem. C* **2017**, *5*, 7684–7698. [[CrossRef](#)]
33. Zhang, Y.; Zheng, Y.; Rui, K.; Hng, H.H.; Hippalgaonkar, K.; Xu, J.; Sun, W.; Zhu, J.; Yan, Q.; Huang, W. 2D Black Phosphorus for Energy Storage and Thermoelectric Applications. *Small* **2017**, *13*, 1700661. [[CrossRef](#)]
34. Hicks, L.D.; Dresselhaus, M.S. Thermoelectric figure of merit of a one-dimensional conductor. *Phys. Rev. B* **1993**, *47*, 16631–16634. [[CrossRef](#)]
35. Shafique, A.; Shin, Y.H. Thermoelectric and phonon transport properties of two-dimensional IV–VI compounds. *Sci. Rep.* **2017**, *7*, 506. [[CrossRef](#)]
36. Babaei, H.; Khodadadi, J.M.; Sinha, S. Large theoretical thermoelectric power factor of suspended single-layer MoS₂. *Appl. Phys. Lett.* **2014**, *105*, 193901. [[CrossRef](#)]
37. Chang, C.; Wu, M.; He, D.; Pei, Y.; Wu, C.F.; Wu, X.; Yu, H.; Zhu, F.; Wang, K.; Chen, Y.; et al. 3D charge and 2D phonon transports leading to high out-of-plane ZT in n-type SnSe crystals. *Science* **2018**, *360*, 778–783. [[CrossRef](#)]
38. Zhao, L.D.; Lo, S.H.; Zhang, Y.; Sun, H.; Tan, G.; Uher, C.; Wolverton, C.; Dravid, V.P.; Kanatzidis, M.G. Ultralow thermal conductivity and high thermoelectric figure of merit in SnSe crystals. *Nature* **2014**, *508*, 373–377. [[CrossRef](#)]
39. Gupta, R.; Kakkar, S.; Dongre, B.; Carrete, J.; Bera, C. Enhancement in the Thermoelectric Performance of SnS Monolayer by Strain Engineering. *ACS Appl. Energy Mater.* **2023**, *6*, 3944–3952. [[CrossRef](#)]
40. Lu, A.Y.; Zhu, H.; Xiao, J.; Chuu, C.P.; Han, Y.; Chiu, M.H.; Cheng, C.C.; Yang, C.W.; Wei, K.H.; Yang, Y.; et al. Janus monolayers of transition metal dichalcogenides. *Nat. Nanotechnol.* **2017**, *12*, 744–749. [[CrossRef](#)]
41. Sa, B.; Sun, Z.; Wu, B. The development of two dimensional group IV chalcogenides, blocks for van der Waals heterostructures. *Nanoscale* **2016**, *8*, 1169–1178. [[CrossRef](#)]
42. Jia, P.Z.; Xie, Z.X.; Deng, Y.X.; Zhang, Y.; Tang, L.M.; Zhou, W.X.; Chen, K.Q. High thermoelectric performance induced by strong anharmonic effects in monolayer (PbX)₂ (X = S, Se, Te). *Appl. Phys. Lett.* **2022**, *121*, 043901. [[CrossRef](#)]
43. Eivari, H.A.; Sohbatzadeh, Z.; Mele, P.; Assadi, M.H.N. Low thermal conductivity: Fundamentals and theoretical aspects in thermoelectric applications. *Mater. Today Energy* **2021**, *21*, 100744. [[CrossRef](#)]
44. Gorai, P.; Stevanović, V.; Toberer, E.S. Computationally guided discovery of thermoelectric materials. *Nat. Rev. Mater.* **2017**, *2*, 17053. [[CrossRef](#)]
45. Kresse, G.; Furthmüller, J. Efficient iterative schemes for ab initio total-energy calculations using a plane-wave basis set. *Phys. Rev. B* **1996**, *54*, 11169–11186. [[CrossRef](#)] [[PubMed](#)]
46. Stratmann, R.E.; Scuseria, G.E.; Frisch, M.J. An efficient implementation of time-dependent density-functional theory for the calculation of excitation energies of large molecules. *J. Chem. Phys.* **1998**, *109*, 8218–8224. [[CrossRef](#)]
47. Kresse, G.; Furthmüller, J. Efficiency of ab-initio total energy calculations for metals and semiconductors using a plane-wave basis set. *Comput. Mater. Sci.* **1996**, *6*, 15–50. [[CrossRef](#)]
48. Kresse, G.; Hafner, J. Ab initio molecular dynamics for liquid metals. *Phys. Rev. B* **1993**, *47*, 558–561; PRB. [[CrossRef](#)]
49. Kresse, G.; Hafner, J. Ab initio molecular-dynamics simulation of the liquid-metal–amorphous-semiconductor transition in germanium. *Phys. Rev. B* **1994**, *49*, 14251–14269; PRB. [[CrossRef](#)]
50. Kresse, G.; Joubert, D. From ultrasoft pseudopotentials to the projector augmented-wave method. *Phys. Rev. B* **1999**, *59*, 1758–1775; PRB. [[CrossRef](#)]
51. Perdew, J.P.; Burke, K.; Ernzerhof, M. Generalized Gradient Approximation Made Simple. *Phys. Rev. Lett.* **1996**, *77*, 3865–3868. [[CrossRef](#)]
52. Monkhorst, H.J.; Pack, J.D. Special points for Brillouin-zone integrations. *Phys. Rev. B* **1976**, *13*, 5188–5192. [[CrossRef](#)]
53. Grimme, S.; Ehrlich, S.; Goerigk, L. Effect of the damping function in dispersion corrected density functional theory. *J. Comput. Chem.* **2011**, *32*, 1456–1465. [[CrossRef](#)]
54. Madsen, G.K.H.; Singh, D.J. BoltzTraP. A code for calculating band-structure dependent quantities. *Comput. Phys. Commun.* **2006**, *175*, 67–71. [[CrossRef](#)]
55. Li, W.; Carrete, J.; A. Katcho, N.; Mingo, N. ShengBTE: A solver of the Boltzmann transport equation for phonons. *Comput. Phys. Commun.* **2014**, *185*, 1747–1758. [[CrossRef](#)]
56. Mouhat, F.; Coudert, F.X. Necessary and sufficient elastic stability conditions in various crystal systems. *Phys. Rev. B* **2014**, *90*, 224104; PRB. [[CrossRef](#)]
57. Bruzzone, S.; Fiori, G. Ab-initio simulations of deformation potentials and electron mobility in chemically modified graphene and two-dimensional hexagonal boron-nitride. *Appl. Phys. Lett.* **2011**, *99*, 222108. [[CrossRef](#)]
58. Fiori, G.; Iannaccone, G. Multiscale Modeling for Graphene-Based Nanoscale Transistors. *Proc. IEEE* **2013**, *101*, 1653–1669. [[CrossRef](#)]
59. Lang, H.; Zhang, S.; Liu, Z. Mobility anisotropy of two-dimensional semiconductors. *Phys. Rev. B* **2016**, *94*, 235306. [[CrossRef](#)]

60. Wang, V.; Xu, N.; Liu, J.C.; Tang, G.; Geng, W.T. VASPKIT: A user-friendly interface facilitating high-throughput computing and analysis using VASP code. *Comput. Phys. Commun.* **2021**, *267*, 108033. [[CrossRef](#)]
61. Rawat, A.; Jena, N.; Dimple.; De Sarkar, A. A comprehensive study on carrier mobility and artificial photosynthetic properties in group VI B transition metal dichalcogenide monolayers. *J. Mater. Chem. A* **2018**, *6*, 8693–8704. [[CrossRef](#)]
62. Shafique, A.; Samad, A.; Shin, Y.H. Ultra low lattice thermal conductivity and high carrier mobility of monolayer SnS₂ and SnSe₂: A first principles study. *Phys. Chem. Chem. Phys.* **2017**, *19*, 20677–20683. [[CrossRef](#)] [[PubMed](#)]
63. Hung, N.T.; Hasdeo, E.H.; Nugraha, A.R.; Dresselhaus, M.S.; Saito, R. Quantum Effects in the Thermoelectric Power Factor of Low-Dimensional Semiconductors. *Phys. Rev. Lett.* **2016**, *117*, 036602. [[CrossRef](#)] [[PubMed](#)]
64. Hung, N.T.; Nugraha, A.R.T.; Yang, T.; Saito, R. Confinement Effect in Thermoelectric Properties of Two-Dimensional Materials. *MRS Adv.* **2020**, *5*, 469–479. [[CrossRef](#)]
65. Li, Y.; Wu, M.N.; Ding, T.; Ma, K.; Liu, F.S.; Ao, W.Q.; Li, J.Q. Promising thermoelectric properties and anisotropic electrical and thermal transport of monolayer SnTe. *Appl. Phys. Lett.* **2019**, *114*, 083901. [[CrossRef](#)]
66. Kumar, S.; Schwingenschlögl, U. Thermoelectric Response of Bulk and Monolayer MoSe₂ and WSe₂. *Chem. Mater.* **2015**, *27*, 1278–1284. [[CrossRef](#)]
67. Patel, A.; Singh, D.; Sonvane, Y.; Thakor, P.B.; Ahuja, R. High Thermoelectric Performance in Two-Dimensional Janus Monolayer Material WS-X (X = Se and Te). *Acs Appl. Mater. Interfaces* **2020**, *12*, 46212–46219. [[CrossRef](#)]

Disclaimer/Publisher's Note: The statements, opinions and data contained in all publications are solely those of the individual author(s) and contributor(s) and not of MDPI and/or the editor(s). MDPI and/or the editor(s) disclaim responsibility for any injury to people or property resulting from any ideas, methods, instructions or products referred to in the content.